Cell Systems

Article

Systematically quantifying morphological features reveals constraints on organoid phenotypes

Highlights

- Quantitative morphometrics can be applied to MDCK cysts
- MDCK cyst morphology has limited dimensionality
- Cyst size scales directly with the number of cells
- Perturbations mostly affect cysts along existing degrees of freedom

Authors

Lauren E. Beck, Jasmine Lee, Christopher Coté, ..., Zev J. Gartner, Prisca Liberali, Arjun Raj

Correspondence

arjunrajlab@gmail.com

In brief

Cells can form complex structures known as organoids that mimic aspects of native tissue morphology. It is unknown, however, what are the constraints this self-organization must obey. Here, Beck et al. use quantitative morphometrics to reveal the constraints on cyst formation by MDCK cells, revealing size and cell number scaling.

Beck et al., 2022, Cell Systems *13*, 1–14
July 20, 2022 © 2022 Elsevier Inc.
https://doi.org/10.1016/j.cels.2022.05.008

CellPress

Please cite this article in press as: Beck et al., Systematically quantifying morphological features reveals constraints on organoid phenotypes, Cell Systems (2022), https://doi.org/10.1016/j.cels.2022.05.008

Cell Systems

CellPress

Article

Systematically quantifying morphological features reveals constraints on organoid phenotypes

Lauren E. Beck,[1] Jasmine Lee,[1] Christopher Coté,[1] Margaret C. Dunagin,[1,2] Ilya Lukonin,[3,4] Nikkita Salla,[1] Marcello K. Chang,[1] Alex J. Hughes,[1,5] Joseph D. Mornin,[6] Zev J. Gartner,[7,8,9] Prisca Liberali,[3,4] and Arjun Raj[1,2,10,*]

[1]Department of Bioengineering, School of Engineering and Applied Sciences, University of Pennsylvania, Philadelphia, PA, USA
[2]Department of Genetics, Perelman School of Medicine, University of Pennsylvania, Philadelphia, PA, USA
[3]Friedrich Miescher Institute for Biomedical Research (FMI), Basel, Switzerland
[4]University of Basel, Basel, Switzerland
[5]Department of Cell and Developmental Biology, Perelman School of Medicine, University of Pennsylvania, Philadelphia, PA, USA
[6]Berkeley, CA, USA
[7]Department of Pharmaceutical Chemistry, University of California, San Francisco, San Francisco, CA, USA
[8]Center for Cellular Construction, University of California, San Francisco, San Francisco, CA, USA
[9]Chan Zuckerberg Biohub, San Francisco, CA, USA
[10]Lead contact
*Correspondence: arjunrajlab@gmail.com
https://doi.org/10.1016/j.cels.2022.05.008

SUMMARY

Organoids recapitulate complex 3D organ structures and represent a unique opportunity to probe the principles of self-organization. While we can alter an organoid's morphology by manipulating the culture conditions, the morphology of an organoid often resembles that of its original organ, suggesting that organoid morphologies are governed by a set of tissue-specific constraints. Here, we establish a framework to identify constraints on an organoid's morphological features by quantifying them from microscopy images of organoids exposed to a range of perturbations. We apply this framework to Madin-Darby canine kidney cysts and show that they obey a number of constraints taking the form of scaling relationships or caps on certain parameters. For example, we found that the number, but not size, of cells increases with increasing cyst size. We also find that these constraints vary with cyst age and can be altered by varying the culture conditions. We observed similar sets of constraints in intestinal organoids. This quantitative framework for identifying constraints on organoid morphologies may inform future efforts to engineer organoids.

INTRODUCTION

Organoids are 3D structures that grow entirely *in vitro* from single or small groups of cells that mimic organ anatomy. Organoids have the potential to transform both personalized and regenerative medicine, since thousands of organoids can be grown under controlled conditions *in vitro* from small amounts of donor tissue. It is clear that organoids can form intricate biological structures, and these structures have an overall structure that resembles the associated organ. Yet, at the same time, there is often enormous variability between individual organoids (Garreta et al., 2021; Koo et al., 2019; Phipson et al., 2019; Kim et al., 2020; Volpato et al., 2018), and changing the organoid culture protocol can similarly lead to large changes (Yin et al., 2014; Sidhaye and Knoblich, 2021; Gjorevski et al., 2016). Thus, the question remains as to what constraints organoids obey to give rise to the aspects of their morphology that are immutable, and what aspects of their morphology are either variable or tunable. Categorizing organoid features in this way may help reveal the design principles underlying organoid development.

One way to formalize the concept of constraints is via the dimensionality of morphospace, which is the set of morphologies an organism or model system can have. If one were to measure all possible features of an organoid's morphology (e.g., size, number of nuclei, together comprising the axes of an organoid's morphospace) across a large enough number of organoids, it could be that a large number of these features would strongly covary and thus could be explained by a single variable. For example, if size and number of nuclei were to be strongly correlated, then the dimensionality would effectively be 1 instead of 2, and the relationship between these variables would constitute a constraint on organoid morphology. On the other hand, if variables show a lack of correlation, then that would suggest independent axes of variability, indicating an additional degree of freedom in organoid morphospace. Examples of such dimension reduction have been demonstrated in both *C. elegans* and Snapdragon flowers, four dimensions capture over 90% of the variance in morphologies (Stephens et al., 2008; Cui et al., 2010). However, such analyses have not been performed in organoids yet. Recent work has quantitatively described brain organoid morphologies (Albanese et al., 2020) and uncovered genetic interactions governing intestinal organoid morphologies (Lukonin et al., 2020), but the constraints on organoid morphologies have not been characterized.

Please cite this article in press as: Beck et al., Systematically quantifying morphological features reveals constraints on organoid phenotypes, Cell Systems (2022), https://doi.org/10.1016/j.cels.2022.05.008

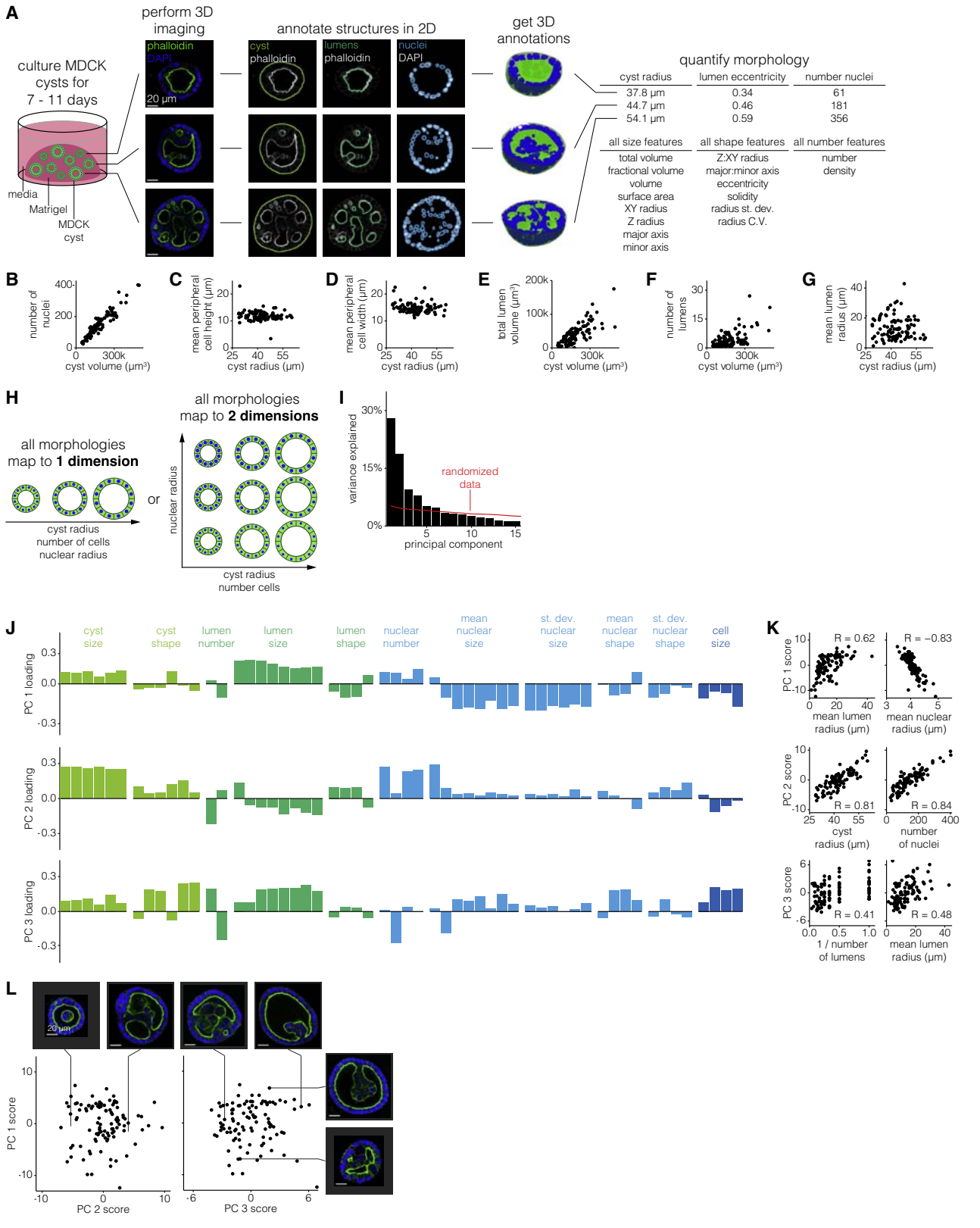

(legend on next page)

Please cite this article in press as: Beck et al., Systematically quantifying morphological features reveals constraints on organoid phenotypes, Cell Systems (2022), https://doi.org/10.1016/j.cels.2022.05.008

One potential reason that there are few quantitative analyses of organoid morphologies is that previous studies have been limited to a small set of two-dimensional features, such as organoid area and nuclear intensity, that fail to fully capture many characteristic aspects of the organoid's shape (Kassis et al., 2019; Gracz et al., 2015). A major challenge is that quantifying morphological features such as the number of cells, cell shapes, etc., often requires microscopy images to be annotated to outline each individual cell or nucleus. While algorithms for automatic segmentation for images of large three-dimensional structures are improving (Piccinini et al., 2020), in many instances, segmentation must still be done manually to ensure sufficient accuracy. Such issues are compounded in organoids with many cell types and complex three-dimensional structures that are difficult to quantitatively align and compare to each other. Simpler "model" organoid systems might serve as a proving ground to test concepts about morphospaces.

How might we characterize the constraints on organoid morphologies? Our approach was to use variation in organoid morphology—both naturally occurring and variation induced by external stimuli—to sample the organoid morphospace. As a proof of concept, we developed this approach in spherical cysts grown from Madin-Darby canine kidney (MDCK) cells. We then quantified morphological features (cyst size, number of cells, eccentricity, etc.) and the relationships between them (how does the number of cells scale with cyst size), thus revealing the constraints on MDCK cyst morphologies. To overcome the challenge of systematically quantifying morphological features, we combined algorithms for generating candidate annotations with software that allowed for quick manual correction. We found that MDCK cyst morphologies all fell along a small set of dimensions. These dimensions encoded a number of constraints; for instance, larger cysts had increased number but not size of constituent cells. We also found that some of these constraints on MDCK cyst morphologies vary with age and can be perturbed through drugs and growth factors. We used quantitative data on enteroid size, cell number, and cell type composition to reveal similar constraints in that more complex organoid system. Our results demonstrate a general strategy for determining the ways in which organoid morphologies are either constrained or free to vary.

RESULTS

MDCK cyst morphologies span a limited number of dimensions

To quantify constraints on cyst morphologies, we designed an experimental and analytical workflow for culturing cysts, performing 3D imaging, annotating structures of interest, and measuring morphological features (Figure 1A). We chose to apply this approach to MDCK cysts because of their relative simplicity and because they are amenable to high magnification 3D imaging. MDCK cells are an immortalized epithelial line that grow in adherent culture on 2D substrates, but form hollow 3D cysts when cultured in 3D matrices such as collagen or Matrigel (Figure S1). A MDCK cyst grows from a single cell and is composed of an outer layer of polarized cells surrounding one to many lumens. The combination of their simplicity with the existence of a number of structural features to quantify make MDCK cysts an ideal system for establishing a framework for quantifying constraints on organoid morphologies.

We evaluated other organoid systems, such as the gut organoids, for our analysis, but found that the complexity of their morphologies presented a much larger challenge. For instance, gut organoids have complex bud structures that one would need to align to each other for quantitative comparison. The comparative simplicity of MDCK cysts that are at least nominally spherical made our analysis feasible as a proof of principle, with MDCK cysts serving as a model for more complex organoids.

In order to quantify 3D measurements of morphological features for hundreds of MDCK cysts, we established a pipeline for semi-automatically annotating cyst structures (nuclei, lumens, and cyst boundary). To identify the lumen and cyst boundaries, we developed a custom analysis pipeline that generated candidate annotations and accepted manual corrections to the annotations as needed (Figure S2). We used cellpose (Stringer et al., 2020) to identify the boundaries of each nucleus and a custom analysis pipeline to manually correct the 3D annotations (Figure S3). Due to depth of field limitations, in many cases we could not image the full depth of the cyst. We thus made sure to image at least the bottom half of the cyst, from which we computationally determined the middle point of each cyst and measured features on only the bottom half of each cyst to ensure a fair comparison between all cysts. We then measured morphological features of size, shape, and number on the nuclei, lumen, and cyst annotations anticipating that these may be the features that vary among cysts (Table S1). We performed a variety of comparisons between morphological features to verify that our measurements were consistent with basic geometric constraints. For example, because the cysts always appeared spherical, we confirmed that the cyst volume scaled with the cube of the cyst radius (Figure S4). We also confirmed that the total lumen and total nuclear volume was always less than that of the cyst volume, and we visually inspected cysts with high

Figure 1. MDCK cyst morphologies span a limited number of dimensions

(A) Schematic of experiments to quantify MDCK cyst morphological features. Briefly, we culture cysts for a variable number of days, perform 3D imaging of nuclei and cell boundaries for at least half of the cyst, annotate the boundaries of the cyst and each nucleus and lumen, and measure morphological features on the 3D annotations. Three MDCK cysts, representative of 64 unperturbed MDCK cysts of age 9 days, are shown for example. Scale bar, 20μm.

(B–G) Comparison of two morphological features for a time-window of 102 7–11-day-old MDCK cysts.

(H) Example schematic of MDCK cyst morphologies that are captured by 1 dimension or 2 dimensions.

(I) Variance explained by each principal component. The red line indicates how much variance is explained when the data is randomized before PCA (see STAR Methods for details).

(J) Loading of each feature on principal components one through three. Each feature is color-coded by what structure (cyst, lumen, nucleus, or cell) it describes.

(K) Correlation between principal component score and raw morphological features for features which highly contribute to that principal component.

(L) Principal component scores for the first three principal components. Each pair of example cysts were chosen because they have high versus low score for one principal component, and similar scores for the other two principal components. Scale bar, 20μm.

Please cite this article in press as: Beck et al., Systematically quantifying morphological features reveals constraints on organoid phenotypes, Cell Systems (2022), https://doi.org/10.1016/j.cels.2022.05.008

and low feature metrics to confirm that the quantified differences reflected differences in the images (Figures S5 and S6).

We then wanted to find relationships between features that could potentially reflect biological constraints. For example, did the number of cells scale with the size of the cyst, as is typically the case in mammalian systems (Hafen and Stocker, 2003; Savage et al., 2007)? Or, did larger cysts have the same number of cells as smaller cysts, but with larger component cells? We used the number of nuclei as a proxy for the number of cells and found that larger cysts had proportionally more nuclei (Figure 1B). Because cells peripheral to the lumen(s) had different morphology than those internal to the lumens, we wondered whether their number scaled differently with cyst volume. We found that the number of peripheral nuclei scaled sublinearly with cyst volume (Figure S7). Surprisingly, the number of internal cells scaled superlinearly with cyst volume, thus ensuring that the total number of cells scaled linearly with cyst volume. Given that the number of cells scaled with the cyst volume, we predicted that cell size should be independent of cyst size. We found that despite increases in cyst volume the peripheral cell height and width are fairly constant at ~9–13 and ~12–18 μm, respectively (Figures 1C and 1D). Together, we called this set of constraints the constant-cell-density constraint.

We also wondered how lumens, both in number and size, scaled with increasing cyst size. For example, if a cyst is larger must it also have larger lumens? One alternative is that there is maximum lumen size, and larger cysts then have multiple lumens of the same size as smaller cysts. We found that the total lumen volume increased with increasing cyst volume, but that this could be achieved through one large lumen or many smaller lumens (Figures 1E–1G). However, we did notice that there was seemingly a maximum number of lumens per cyst that increased linearly with cyst volume. We called this constraint the "lumen number cap," and its existence suggests that there may be a minimum lumen size (Figure S8).

Given that MDCK cysts obey a number of constraints, we then wondered whether these constraints are coupled. In other words, might there be a single dimension (or a few dimensions), each of which may comprise several correlated features, along which all MDCK cyst morphologies fall (Figure 1H)? To identify dimensions in the space of MDCK cyst morphologies we performed principal component analysis (PCA) on the set of 77 cysts and their 66 morphological features. In order to apply PCA to our data, we needed to supply a single value for each feature for each cyst. For all features describing nuclei we used both the mean and standard deviation across all nuclei within the cyst, e.g., mean nuclear volume and standard deviation of nuclear volume. For features describing lumens we used the mean across all lumens in the cyst, e.g., mean lumen volume. We did not include other higher order statistics like standard deviation because it was impossible to do so for the many cysts that had only one lumen. We found that the first three principal components respectively explain 28%, 19%, and 10% of the variation in MDCK cyst morphologies (Figure 1I). We then wondered whether the principal components (PCs) reflected any of the constraints we had previously identified. We found that the first principal component represented lumen size and inversely nuclear size, reflecting the fact that as lumens get larger, nuclei get smaller (Figures 1J–1L and S9). Note that this trend is consistent with our earlier finding of relatively constant cell size because cell size and nuclear size are different properties. The second principal component represents cyst size and number of nuclei, reflecting that increased cyst size was associated with increased number of nuclei, a relationship we previously identified as the constant-cell-density constraint. The third principal component represented the trade-off between lumen size and the number of lumens, reflecting that, for a given cyst size, to have more lumens, the individual lumens must be smaller (rather than there is a maximum lumen size which is independent of the number of lumens). The third principal component also represented a trade-off between nuclear size and the density of nuclei, reflecting that, for a given cyst size, to have more nuclei the nuclei must be smaller (Figure S10). Consistent with PC1, we also found that nuclear size anti-correlated with lumen size. Beyond those three principal components, the remaining components accounted for less variation than components calculated from randomized data, suggesting that those PCs likely do not reflect substantial variation in the data. In addition to performing conventional PCA on our data, we also used a sparse PCA method (Benjamin Erichson et al., 2018), which can aid with interpretation because it tries to reduce small contributions to principal components to zero when possible. We found that the principal components from such an analysis (after discarding the first principal component, which is most likely technical and batch variability) recapitulated similar contributions to the axes of variation revealed by conventional PCA. This analysis also had a more straightforward interpretation owing to the principal components having just a few primary contributing features (Figure S11). Thus, despite quantifying a large number of features, MDCK cyst morphologies can thus be represented by a limited number of dimensions.

Constraints on MDCK cyst morphologies vary with age

MDCK cysts grow continuously over the course of weeks, from a single cell into large cysts. To determine whether or not cyst age affected the constraints on MDCK cyst morphologies, we compared the quantitative relationship between various features for cysts of different ages. We partitioned our data based on cyst age, ranging from 3 to 17 days of growth. Using the same imaging and feature quantification described above, we saw that, as expected, old cysts were larger in volume on average (Figures 2A and 2B). We also noticed that, for a given age, there was a spread in cyst sizes. This variation in size enabled us to compare constraints in cyst size across different age categories (Figure 2C). We used cysts cultured for 9 days as a reference point for younger and older cysts to evaluate how constraints on MDCK cyst morphologies changed with cyst age.

We first wondered if the constant-cell-density constraint varied for cysts of different ages (Figures 2D and S12). We found that cysts of all ages obeyed the constant-cell-density constraint on the number of nuclei and cyst volume. This relationship was confirmed by PCA run on the complete dataset including all time points, in which the principal components remained the same, but the principal component for cyst size accounted for more total variance due to size differences with age (Figure S13). However, the exact nature of this constraint, specifically the slope and intercept of the linear relationship, varied with the age of the cyst. Cysts cultured for 3–5 or 13–17 days obeyed a

Please cite this article in press as: Beck et al., Systematically quantifying morphological features reveals constraints on organoid phenotypes, Cell Systems (2022), https://doi.org/10.1016/j.cels.2022.05.008

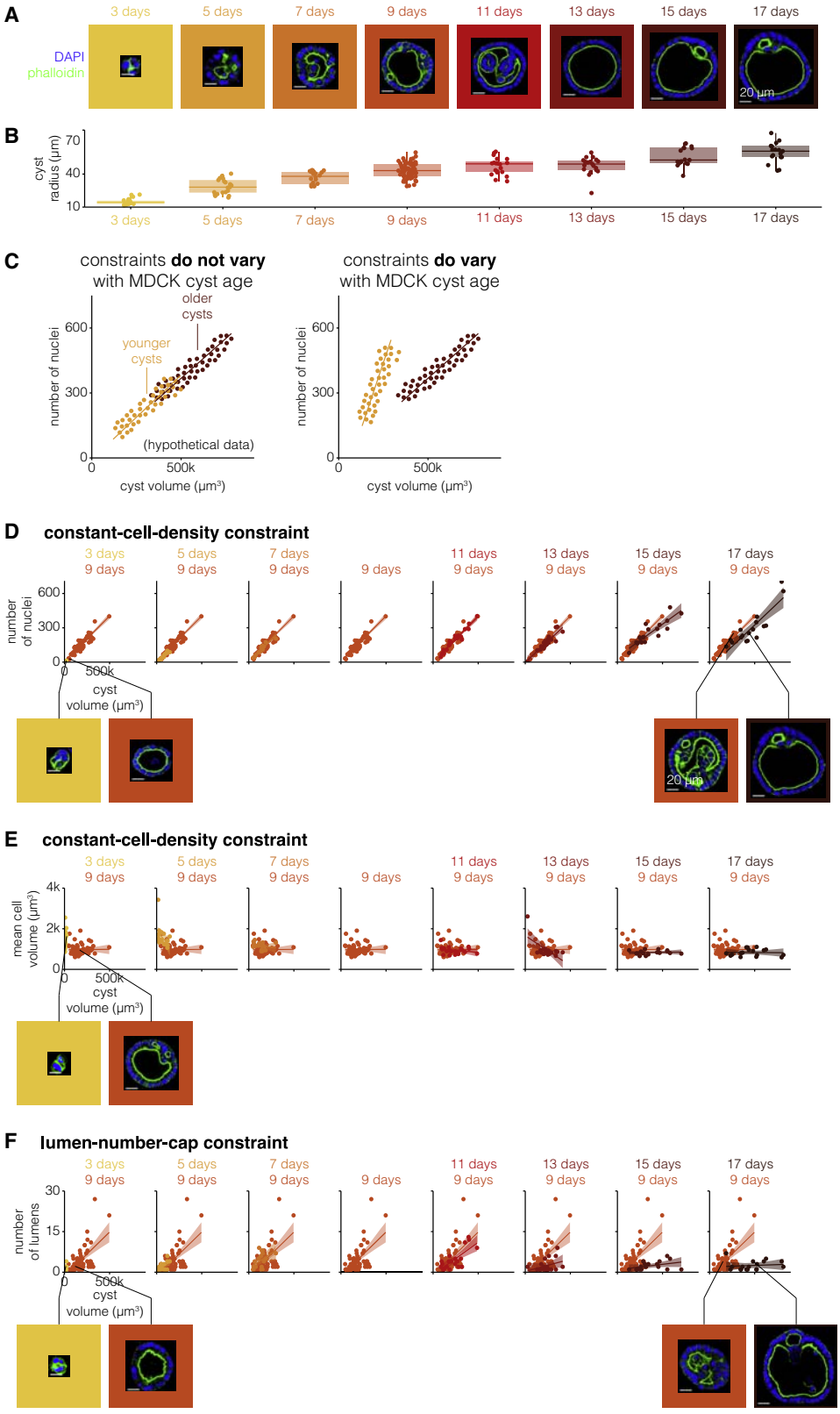

Figure 2. Constraints on MDCK cyst morphologies vary with age

(A) One example MDCK cyst for each age (representative of 17–64 MDCK cysts of the same age). The MDCK cyst shown is one with approximately average radius for that age. Scale bar, 20μm.

(legend continued on next page)

Please cite this article in press as: Beck et al., Systematically quantifying morphological features reveals constraints on organoid phenotypes, Cell Systems (2022), https://doi.org/10.1016/j.cels.2022.05.008

constant-cell-density constraint with a smaller slope; i.e., they had fewer nuclei per cyst volume. As cysts age, they get larger, so in principle it could be that older cysts could have a lower cell density because all cells are larger, or it could be that there is a threshold volume beyond which cell density decreases. We found that among older cysts with smaller sizes (that matched those of middle-aged cysts), the densities were similar to those of middle-aged cysts, suggesting the latter threshold scenario (Figures 2E and S14). Younger cysts, however, had a uniformly lower cell density than middle-aged cysts.

We wondered whether other constraints were similarly affected by age. We looked at the age dependence of the lumen-number-cap constraint (Figures 2F and S15). We again found that cysts of all ages obeyed a constraint on the number of lumens per cyst volume. However, this constraint changed with age: we found that younger cysts cultured for 3 days had a higher maximum number of lumens per cyst volume, and cysts cultured for 13–17 days had a lower maximum number of lumens per cyst volume. The decrease in the number of lumens per cyst as cysts age beyond 9 days suggests that multiple lumens in a cyst are either merging or disappearing as cysts grow older. It is difficult to speculate what mechanisms might govern this age-dependent quantitative change in constraints without perturbations. However, given that very young cysts seem to obey an entirely different set of constraints than older cysts, it may be that some of these differences are due to the establishment of apico-basal polarity around the lumen considering the work of Vasquez et al. (Vasquez et al., 2021). Also, we noticed in young cysts that the threshold of size and number of nuclei to form a lumen was 10,000 μm^3 and 7 nuclei, respectively (Figure S16). Together, our results point to constraints as being dynamic entities that can change as cysts grow and develop.

Drug and environmental perturbations can change constraint parameters but do not break them

Having found constraints on MDCK cyst morphologies, we wondered whether these constraints applied to cysts whose morphology we perturbed using exogenous agents. For example, if we perturb the cysts with a drug which makes the cysts larger, will the same constant-cell-density constraint still apply? If not, there are two ways that the constraint could be disobeyed. One is that the perturbed cysts could follow the same constraint but with different parameters, for example, by changing the slope of the relationship between cell number and cyst volume. Alternatively, a perturbation could qualitatively remove a constraint and decouple, for example, the number of nuclei and cyst volume. Either of these possibilities would suggest that the constraints on MDCK cyst morphologies are context-specific.

There are few references to drugs which modify the morphology of MDCK cysts in the literature. Thus, to identify drugs that change MDCK cyst morphologies we designed a high-throughput drug screen of small molecule drugs from Selleck Chemicals Bioactive Compound library. This library contains ~2,000 small molecule drugs including kinase and epigenetic inhibitors as well as ion channel, metabolic, and cancer compounds. To conduct the screen, we plated MDCK cells in 384-well plates, added 1 μM of each drug, and allowed the cells to grow into cysts for 7 days, at which point the cysts were fixed and imaged. We then quantified the area of each cyst and the average across cysts for each perturbation. We found that, while most drugs did not appear to change the area of the cyst relative to controls, there were many drugs which made the cysts smaller or larger (Figure 3A). We considered "hits" for larger cysts to be the drugs that were on both the list of the top 100 drugs as ranked by fold change and the list of the top 100 drugs as ranked by Z score, a total of 78 drugs. We found 80 "hits" for smaller cysts using the same approach. We found that hits that resulted in smaller cysts were enriched for drugs in the kinase, epigenetic, and cancer categories, while hits for larger cysts were enriched for kinases, cancer, and G protein-coupled receptor categories (Figure S17). To gauge how many of our hits may have arisen by chance, we screened a portion (1/7th) of the drug library again. We found that there was a correlation ($r = 0.63$) between the fold change in cyst area from the screen and this targeted replication, suggesting that the majority of our hits were not random (Figure S18). The screen hits represented potential candidates for perturbing MDCK cyst morphologies and then asking whether perturbed MDCK cysts obey the same constraints as unperturbed cysts.

We further manually grouped hits for smaller and larger cysts according to their targets (Tables S3 and S4). We selected four drugs from our list of hits from the screen that increased cyst size from groups targeting mammalian target of rapamycin, aurora kinase, phosphodiesterase, and serotonin. Similarly, we selected three drugs that made cysts smaller from groups targeting epidermal growth factor receptor, histone deacetylases, and exportin-1. Given the relatively small number of factors we were able to rigorously test, we did not perform enrichment analysis on the categories of factors that came up as targets of our drug screen. We additionally used the following perturbations we thought likely to change MDCK cyst morphology based on the literature: idelalisib, oratinib, Y-27632, NSC23766, and blebbistatin. We plated MDCK cells to form cysts, immediately

(B) Quantification of cyst radius for 17–64 MDCK cysts of different ages.
(C) Example of a constraint that does or does not vary with MDCK cyst age for hypothetical data.
(D) Number of nuclei versus cyst volume for 17–64 MDCK cysts of each age. Each age is represented by one color, and 9-day-old MDCK cysts are repeated on each graph for reference. The line represents the line of best fit and the shaded area represents the 95% confidence interval. Example MDCK cysts with approximately the same number of nuclei but different volumes. Scale bar, 20μm.
(E) Mean cell volume versus cyst volume for 17–64 MDCK cysts of each age. Each age is represented by one color, and 9-day-old MDCK cysts are repeated on each graph for reference. The line represents the line of best fit and the shaded area represents the 95% confidence interval. Example MDCK cysts with approximately the same volume but different mean cell volumes. Scale bar, 20μm.
(F) Number of lumens versus cyst volume for 17–64 MDCK cysts of each age. Each age is represented by one color, and 9-day-old MDCK cysts are repeated on each graph for reference. The line represents the line of best fit and the shaded area represents the 95% confidence interval. Example MDCK cysts with approximately the same number of lumens but different cyst volumes. Scale bar, 20μm.

Please cite this article in press as: Beck et al., Systematically quantifying morphological features reveals constraints on organoid phenotypes, Cell Systems (2022), https://doi.org/10.1016/j.cels.2022.05.008

CellPress

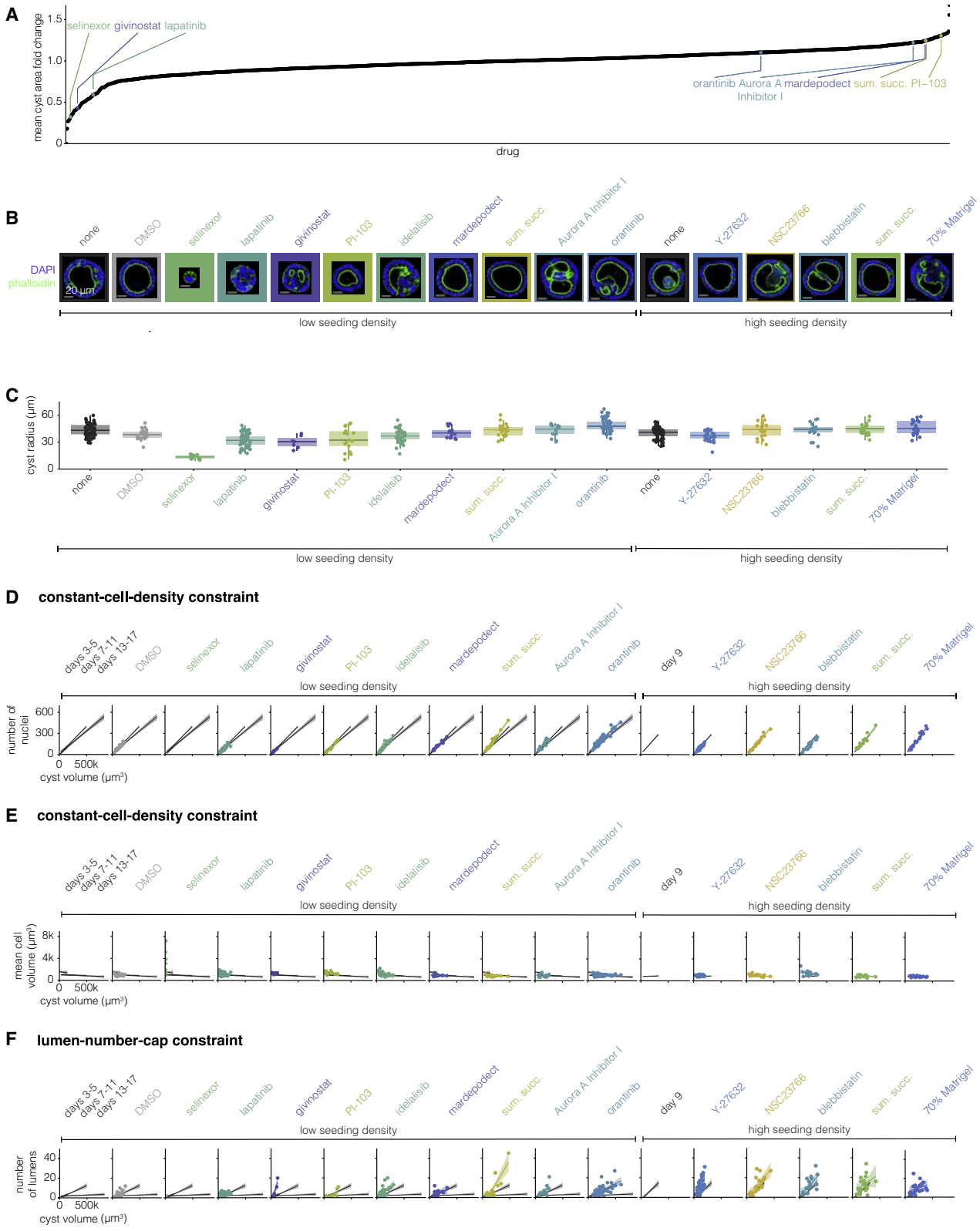
A
mean cyst area fold change
selinexor givinostat lapatinib
orantinib Aurora A Inhibitor I mardepodect sum. succ. PI–103
drug
B
none DMSO selinexor lapatinib givinostat PI-103 idelalisib mardepodect sum. succ. Aurora A Inhibitor I orantinib none Y-27632 NSC23766 blebbistatin sum. succ. 70% Matrigel
DAPI
phalloidin
20 µm
low seeding density
high seeding density
C
cyst radius (µm)
low seeding density
high seeding density
D
constant-cell-density constraint
days 3-5 days 7-11 days 13-17 DMSO selinexor lapatinib givinostat PI-103 idelalisib mardepodect sum. succ. Aurora A Inhibitor I orantinib day 9 Y-27632 NSC23766 blebbistatin sum. succ. 70% Matrigel
low seeding density
high seeding density
number of nuclei
cyst volume (µm³)
E
constant-cell-density constraint
mean cell volume (µm³)
cyst volume (µm³)
F
lumen-number-cap constraint
number of lumens
cyst volume (µm³)

(legend on next page)

Please cite this article in press as: Beck et al., Systematically quantifying morphological features reveals constraints on organoid phenotypes, Cell Systems (2022), https://doi.org/10.1016/j.cels.2022.05.008

added these drugs at a range of concentrations, and then grew the cysts for 9 days (Table S2). Additionally, we tested two non-drug perturbations, cell seeding density (by culturing MDCK cysts with a higher initial cell density) and dilute Matrigel. We then fixed, stained, and imaged the perturbed cysts as described above, after which we measured the same set of morphological features (Figures 3B and 3C). We found that the screen hits that we expected to make cysts smaller did indeed lead to smaller cysts, but none of the ones predicted to make them larger did so. We found that increased seeding density nor dilute Matrigel had no effect on the size of the cysts. Note that many of the hits from the screen targeted proliferation, suggesting that perhaps effects on size were a necessary consequence of changes to proliferative capacity. However, many other drugs in the screen also targeted proliferation but had no effect on cyst size, arguing against this possibility.

We then wondered whether perturbed cysts obeyed the same constant-cell-density and lumen-number-cap constraints as unperturbed cysts. We found that, with the exception of five drugs, perturbed cysts obeyed the same constant-cell-density constraint as unperturbed cysts (Figures 3D and 3E). Cysts perturbed with sumatriptan succinate (a serotonin receptor inhibitor) or blebbistatin (a myosin II inhibitor) had more nuclei per given cyst volume than any age of unperturbed cysts. Cysts perturbed with selinexor (an exportin-1 inhibitor), Y-27632 (a ROCK inhibitor), NSC 23766 (a Rac inhibitor), or blebbistatin had larger nuclei per given cyst volume. Notably, the relationship between cell number, size, and cyst volume is still constrained for cysts perturbed with any of these drugs, but the parameters of the constraint (specifically the slope) are different from unperturbed cysts.

We then wondered how a perturbation which does change a constraint influences other constraints—if cysts perturbed with drug X do not obey the constant-cell-density constraint, must they also not obey the lumen-number-cap constraint? We found that cysts perturbed with givinostat (a histone deacetylase inhibitor), idelalisib (a phosphoinositide 3-kinase delta isoform inhibitor), sumatriptan succinate, Aurora A Inhibitor I, Y-27632, and blebbistatin had more lumens in a given cyst volume than unperturbed cysts of any age (Figure 3F). Thus, cysts perturbed with these drugs do not obey the same lumen-number-cap constraint of unperturbed cysts, instead they obey a constraint with a larger slope. We found that some perturbations (selinexor, givinostat, idelalisib, Aurora A Inhibitor I, and NSC 23766) changed only one constraint, but others (sumatriptan succinate, Y-27632, and blebbistatin) changed both. Given the targets of these perturbations, we can hypothesize as to which mechanisms may regulate these constraints. We saw that exportin 1 was important for the constant-cell-density constraint, histone deacetylases, PI3K, and Aurora A kinase for the lumen-number-cap constraint, and serotonin receptors were important to both constraints. We similarly found some mechanisms perturbed MDCK cysts along a single axis in principal component space, while others perturb cysts along two axes (Figure S19), suggesting that the axes of MDCK cyst variation may not be governed by independent mechanisms. These factors all work through quite different pathways; however, given the relatively small number of perturbations we analyzed, it was difficult to uncover any general rules on which pathways affected which constraints. In combination, this suggests that the set of morphologies available to MDCK cysts is richer than unperturbed cysts would suggest.

Constraints of perturbed cysts do not add together or average out when multiple perturbations are applied

Exposing MDCK cysts to hepatocyte growth factor (HGF) in collagen gels induces cells to send out spindly extensions (Montesano et al., 1991b, 1991a). These extensions form the groundwork for a chain of cells to proliferate and ultimately form tubules. We wondered how such a perturbation might change the constraints on cyst morphologies we identified, given that it leads to known, qualitative changes in cyst morphology. We added HGF to MDCK cysts as they grew for nine days (Figure 4A). We used our imaging and feature quantification approach to characterize the constraints on cysts exposed to HGF. We asked whether our measurements of cyst shape captured the morphology of extensions in HGF-perturbed cysts. We found that one of the primary differences between unperturbed and HGF-perturbed cysts was cyst solidity, a measure of convexity (cysts with more involutions or protrusions have lower solidity than circular or elliptical cysts) (Figures 4B and S20). Mean cyst solidity decreased from 0.93 for unperturbed cysts to 0.75 for HGF-perturbed cysts. We also found that cysts exposed to HGF were larger, on average, than unperturbed cysts (Figure 4C).

Given the qualitative difference in morphology of HGF-perturbed cysts, we wondered if HGF-perturbed cysts obeyed the constraints obeyed by unperturbed MDCK cysts. We found that HGF-perturbed cysts did not obey both aspects of the

Figure 3. Drug and environmental perturbations can change constraint parameters but do not break them

(A) Fold change in cyst area versus each drug from the screen. Annotated drugs are those used in further experiments.

(B) One example MDCK cyst for each perturbation (representative of 7–65 MDCK cysts of the same perturbation). The MDCK cyst shown is one with approximately average radius for that perturbation. The seeding cell density, low (25,000 cells/mL) or high (1,00,000 cells/mL), and the drug added to the culture media are indicated below the image.

(C) Quantification of cyst radius for 7–65 MDCK cysts exposed to different perturbations.

(D) Number of nuclei versus cyst volume for 7–65 MDCK cysts exposed to different perturbations. Each perturbation is represented by one color. The line represents the line of best fit and the shaded area represents the 95% confidence interval. The line of best fit and 95% confidence interval for three groups of unperturbed MDCK cysts (3–5, 7–11, and 13–17 days) are shown in gray for reference.

(E) Mean cell volume versus cyst volume for 7–65 MDCK cysts exposed to different perturbations. Each perturbation is represented by one color. The line represents the line of best fit and the shaded area represents the 95% confidence interval. The line of best fit and 95% confidence interval for three groups of unperturbed MDCK cysts (3–5, 7–11, and 13–17 days) are shown in gray for reference.

(F) Number of lumens versus cyst volume for 7–65 MDCK cysts exposed to different perturbations. Each perturbation is represented by one color. The line represents the line of best fit and the shaded area represents the 95% confidence interval. The line of best fit and 95% confidence interval for three groups of unperturbed MDCK cysts (3–5, 7–11, and 13–17 days) are shown in gray for reference.

Please cite this article in press as: Beck et al., Systematically quantifying morphological features reveals constraints on organoid phenotypes, Cell Systems (2022), https://doi.org/10.1016/j.cels.2022.05.008

CellPress

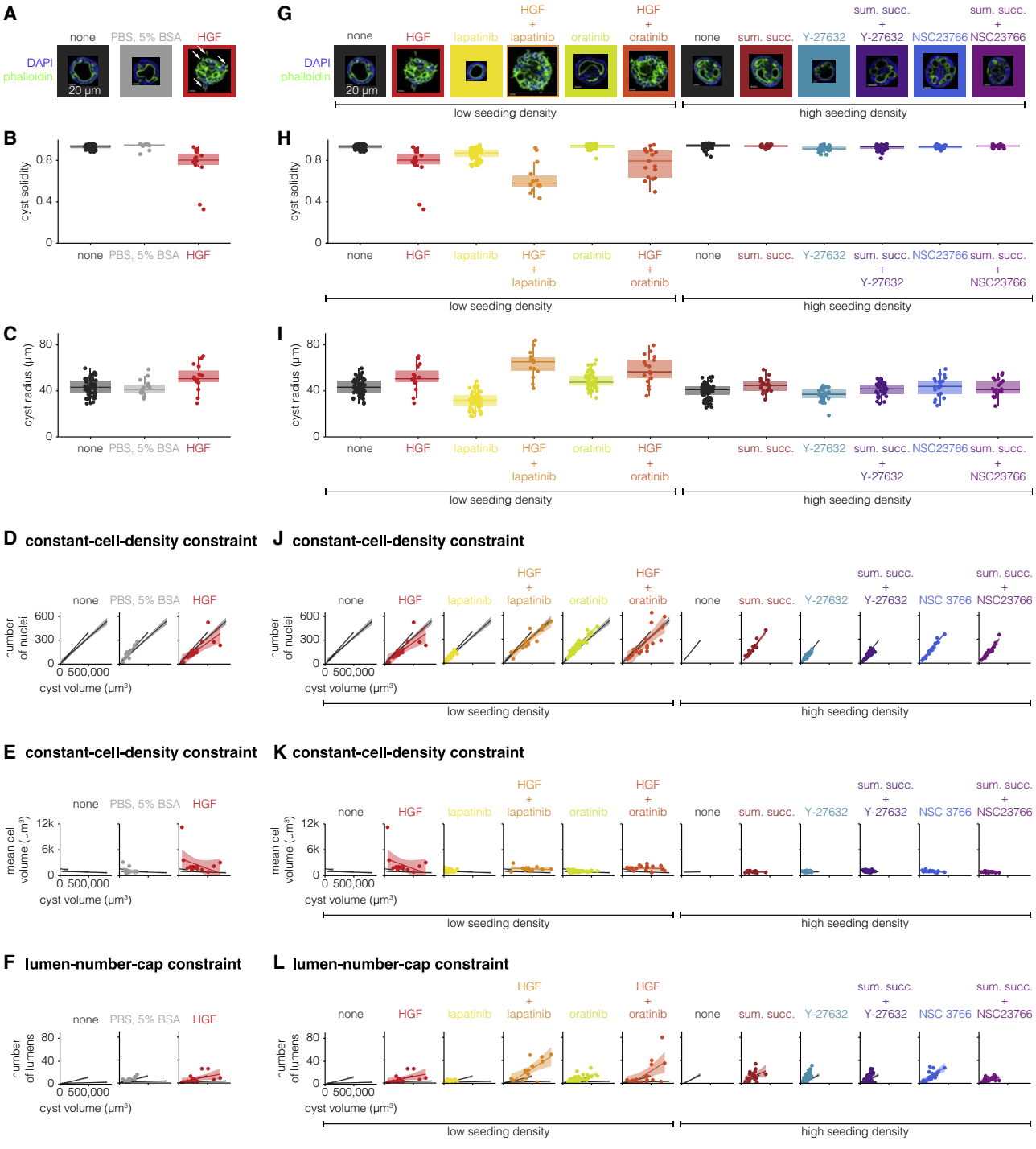

Figure 4. Constraints of perturbed cysts do not add together or average out when multiple perturbations are applied

(A and G) One example MDCK cyst for each perturbation (representative of 15–65 MDCK cysts of the same perturbation). The MDCK cyst shown is one with approximately average radius for that perturbation. The seeding cell density, low (25,000 cells/mL) or high (1,00,000 cells/mL), and the drug added to the culture media are indicated below the image. White arrows indicate spindle-like extensions. Scale bar, 20μm.

(B and H) Quantification of cyst solidity for 15–65 MDCK cysts exposed to different perturbations.

(C and I) Quantification of cyst volume for 15–65 MDCK cysts exposed to different perturbations.

(D and J) Number of nuclei versus cyst volume for 15–65 MDCK cysts exposed to different perturbations. Each perturbation is represented by one color. The line represents the line of best fit and the shaded area represents the 95% confidence interval. The line of best fit and 95% confidence interval for three groups of unperturbed MDCK cysts (3–5, 7–11, and 13–17 days) are shown in gray for reference.

(legend continued on next page)

Please cite this article in press as: Beck et al., Systematically quantifying morphological features reveals constraints on organoid phenotypes, Cell Systems (2022), https://doi.org/10.1016/j.cels.2022.05.008

constant-cell-density constraint: while cysts perturbed with HGF had the same number of cells per cyst volume, the cells were larger than those of unperturbed cysts of any age (Figures 4D and 4E). How do HGF-perturbed cysts have the same number of cells per cyst volume, but larger cells than unperturbed cysts? One possibility was that HGF-perturbed cysts have a smaller proportion of their volume taken up by lumens and a larger proportion of the volume occupied by cells. Interestingly, HGF-perturbed cysts do obey the lumen-number-cap constraint, suggesting that what lumens HGF-perturbed cysts have are smaller in size but similar in number (Figure 4F). The smaller proportion of volume taken up by the lumens could result from cells being taller or adopting a different configuration. We found that the cells often formed multi-cell layers, which allows for larger cells to occupy the same organoid volume while maintaining the same total number of cells per volume. It also suggests that the strict proportionality between cell number and organoid volume is maintained despite disruptions to cellular configurations and hence cell number may not be controlled by morphology per se.

Given that HGF qualitatively changed some features of MDCK cysts, we wondered what the morphological effects would be upon combining HGF with the previously used perturbations that engendered more quantitative changes. For example, would a perturbation that produces cysts with extensions (HGF) and a perturbation that produces smaller cysts yield small cysts with extensions? We perturbed MDCK cysts for nine days with either HGF alone or HGF in combination with lapatinib or orantinib (Figure 4G). To ensure that any differences we noticed could not be explained by possible cross-talk between HGF and epidermal growth factor receptor (Jo et al., 2000), we additionally perturbed MDCK cysts with sumatriptan succinate alone or in combination with Y-27632 or NSC23766. We found that cysts exposed to HGF and lapatinib or oratinib had lower solidity than cysts exposed to only one of these perturbations (Figure 4H). We found that cysts exposed to HGF, alone or in combination, were also larger, on average, than control cysts (Figure 4I). Taken together, the morphological changes induced by HGF and another perturbation suggest that the effects of individual perturbations do not necessarily combine additively when administered simultaneously.

We then wondered how the constraints of cysts perturbed with one drug changed when the cysts were exposed to a second drug. One possibility is that doubly-perturbed cysts obeyed a set of constraints that averaged the constraints obeyed by singly-perturbed cysts (assumption of linearity). Another possibility is that doubly-perturbed cysts obeyed the same set of constraints as only one of the perturbations, suggesting that some drugs may be able to override the effects of others, or some other nonlinear interaction. One might expect that linearity would hold for small doses of drug, but that nonlinear aspects of the regulatory processes may appear for larger doses. We found that sometimes one perturbation overrode the effects of the other and that sometimes doubly-perturbed cysts did not obey the same constraints that the singly-perturbed cysts did (Figures 4J–4L). Perturbations overrode the effects of one another in many combinations and for both constraints. We observed that while HGF alone obeyed a different constant-cell-density constraint, when used in combination with either lapatinib or oratinib the cysts obeyed the same constraint as unperturbed cysts. We likewise found that the effects of Y-27632 on the lumen-number-cap constraint and the effects of NSC23766 on the constant-cell-density constraint were both canceled out by sumatriptan succinate. We additionally found many examples where singly-perturbed MDCK cysts obeyed the same constraints, but when those perturbations were used in combination the cysts did not obey the same constraints. We found that while neither HGF, lapatinib, nor oratinib alone changed the lumen-number-cap constraint, cysts perturbed with both HGF and lapatinib or oratinib had higher lumens per cyst volume (Figures 4J–4L). We also found this to be true for sumatriptan succinate and Y-27632 for the constant-cell-density constraint. In totality, the many differences between the constraints obeyed by double-perturbed cysts and single-perturbed cysts suggests that the effects of any given perturbation do not appear to simply add together, but rather can combine in unanticipated ways. It is important to note that many of the perturbations affected particular classes of biological processes, such as proliferation (e.g., lapatinib, oratinib, etc.) and those affecting morphological processes (e.g., HGF, Y-27632, etc.). It is possible that the use of different combinations with drugs perturbing the same processes could have more predictable effects.

Enteroids show a similar set of perturbable constraints

The MDCK cyst formation system is relatively simple (spherical shape, single cell type), and so we wondered whether our approach would apply to more complex organoid systems. We chose to apply our approach to the enteroid system, which is an organoid system mimicking intestinal crypt and villus structures. In this system, enteroids can be derived from a single intestinal epithelial stem cell, from which multiple cell types emerge to form a structure that in some ways reflects the crypt and villus structure of the intestinal epithelium. In that structure, stem cells are at the base of the crypt and give rise to the other cell types, including Paneth cells, goblet cells, enterocytes, transit amplifying cells, and enteroendocrine cells (Figure 5A). In Lukonin et al. (2020), the authors performed high-throughput quantitative measurements on enteroids exposed to a wide variety of perturbative conditions (2,455 conditions), generating a dataset that matched many of the criteria for our approach. Their measurements included enteroid area and a number of associated morphological quantities (Figure 5B). Furthermore, they performed antibody staining for markers of Paneth cells and enterocytes, along with nuclear staining with DAPI, yielding the

(E and K) Mean cell volume versus cyst volume for 15–65 MDCK cysts exposed to different perturbations. Each perturbation is represented by one color. The line represents the line of best fit and the shaded area represents the 95% confidence interval. The line of best fit and 95% confidence interval for three groups of unperturbed MDCK cysts (3–5, 7–11, and 13–17 days) are shown in gray for reference.
(F and L) Number of lumens versus cyst volume for 15–65 MDCK cysts exposed to different perturbations. Each perturbation is represented by one color. The line represents the line of best fit and the shaded area represents the 95% confidence interval. The line of best fit and 95% confidence interval for three groups of unperturbed MDCK cysts (3–5, 7–11, and 13–17 days) are shown in gray for reference.

Please cite this article in press as: Beck et al., Systematically quantifying morphological features reveals constraints on organoid phenotypes, Cell Systems (2022), https://doi.org/10.1016/j.cels.2022.05.008

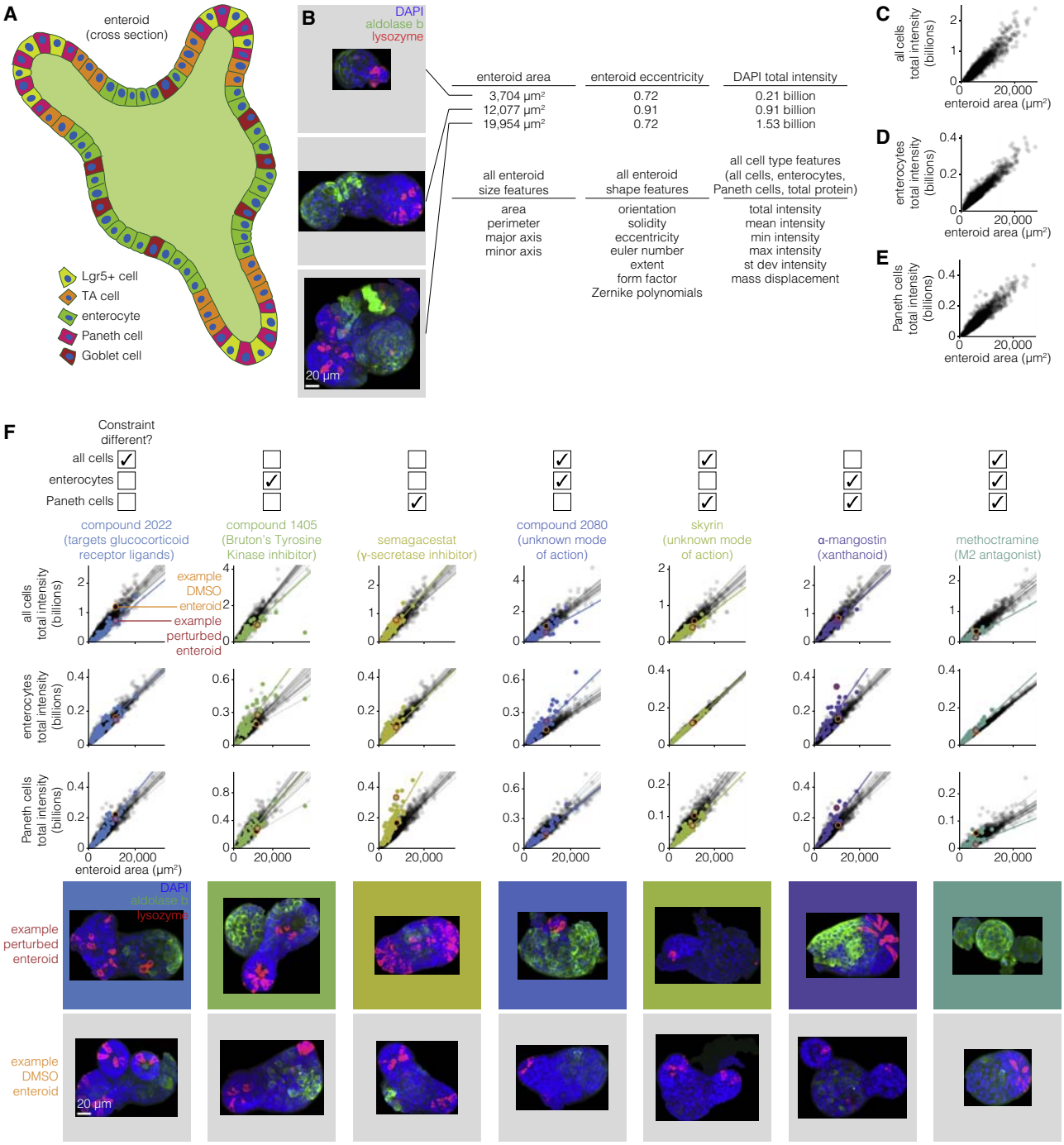

Figure 5. Enteroids obey a similar set of constraints that can also be modulated by drugs

(A) Schematic of enteroid with different cell types identified.

(B) Example enteroids with different morphological and cell type features. Three enteroids, representative of the range of sizes and shapes seen across 33,304 unperturbed enteroids, are shown for example. Scale bar, 20μm.

(C) Total intensity of all cells versus cyst volume for 33,304 unperturbed enteroids.

(D) Total intensity of enterocytes versus cyst volume for 33,304 unperturbed enteroids.

(E) Total intensity of Paneth cells versus cyst volume for 33,304 unperturbed enteroids.

(F) Constraints from (C)–(E) for 36–128 enteroids perturbed with drugs. An example perturbation is shown for each set of constraints that can be different. 1,103–1,889 unperturbed enteroids are plotted in gray and perturbed enteroids are plotted in color. The lines represent the line of best fit and are plotted for each well that the enteroids were cultured in. The enteroids in the images are circled on the graph (unperturbed enteroid in orange and perturbed enteroid in red). Scale bar, 20μm.

Please cite this article in press as: Beck et al., Systematically quantifying morphological features reveals constraints on organoid phenotypes, Cell Systems (2022), https://doi.org/10.1016/j.cels.2022.05.008

fluorescence intensity of these markers as a proxy for the number of cells of these types (and total cells in the case of DAPI). It is worth noting here that while the intensities serve as a proxy for cell number, they do not give the relative location of these cell types, which are data that could be useful in future studies.

We first performed PCA on the features from this enteroid dataset to look for constrained covariation between features (Figure S21). We found that there were several principal components that appeared to explain a significant fraction of the variance. The first principal component appeared to correspond to size, and again revealed a strong correlation between size and total number of cells as well as the number of enterocytes and Paneth cells. Looking at the second and third principal components, the density (or mean intensity) of Paneth cells appeared to correlate with protein density and density of cells independently of any enterocyte features (PC2). However, the density of enterocytes seemed to correlate with protein density independent of all cell and Paneth cell features (PC3). Together, the PCA revealed a number of axes of variation with respect to the relative numbers of different cell types.

We first wanted to establish that the scaling properties that we observed in MDCK had some analogy in the enteroid system (Figures 5C–5E). We found that all three fluorescence intensity quantities (DAPI/number of nuclei, aldolase b/number of enterocytes, lysozyme/number of paneth cells) scaled strongly with enteroid area, showing that the numbers of each of these cell types in general scaled with the total size of the enteroid. Note that the nature of these data was rather different than that collected for MDCK, so we performed a different set of quality control steps; see STAR Methods for details.

With these strong linear relationships in hand, we went about searching through the set of perturbations looking for examples of perturbations that altered these relationships and combinations thereof. We looked for perturbations that gave large fold changes to the slope or intercept of a linear fit as compared with unperturbed enteroids, with the further criterion that the majority of replicates of the drug (both replicates when there were two total replicates, or at least two out of three if there were three total replicates) must show the change (Figure 5F). We found 118 perturbations that caused a change in at least one of the constraints. We confirmed these changes by looking at the raw images, which demonstrated that the changes in fluorescence intensity resulted from changes in the number of cells of the various types predicted (as opposed to changes in staining intensity of the same number of cells). Indeed, for the seven possible combinations of constraint changes (changes in 1, 2 or all 3 of the constraints at once), we found at least one perturbation (often several) for each constraint change combination. Our results show that the scaling property of the number of cells of a particular type with organoid size are maintained across perturbations, but that the scaling constant itself (i.e., the proportion of cells of a particular type out of the total) are subject to change.

In conclusion, we found that our approach was able to identify constraints in a more complex organoid system, and that these constraints were perturbable. It is important to note that the set of features in these data is likely far richer than what was currently captured in our measurements; for instance, quantities associated with the distances between various cell types were not computed. A richer set of features may lead to a richer set of constraints.

DISCUSSION

Here, we sought to quantify constraints on MDCK cyst morphologies. We found the MDCK cysts obey a number of constraints, and that the majority of their morphological variation can be explained by three dimensions. We also found that some constraints on MDCK cyst morphologies vary with age and perturbations.

It remains unclear what underpins the constraints on cyst (or, more generally, organoid) morphologies. One could imagine any number of potential mechanisms, any one of which might be critical to a constraint by itself or in combination with many others. Such mechanisms may be based upon conventional biochemical signaling (such as signaling between cells to control proliferation), or may involve mechanical sensing of variables such as membrane curvature. A related question is whether these mechanisms map in a one-to-one manner onto each of the principal components of variation we detected. That is, is there one mechanism that governs cell size and related variables, and another mechanism that governs lumen number? In principle, there is no need for any one mechanism to map in such a direct way onto a particular axis of variation. Our data with various drugs suggests that it is entirely possible for a mechanism to affect just one or multiple principal components, so there is no reason to predict that individual mechanisms would be restricted to affecting just a single axis.

While many potential mechanisms may be compatible with our experimental data, perturbations will be required to exclude certain classes of models and establish causality. Such molecular mechanisms, if identified, are enormously powerful and are a critical ultimate goal for molecular biology. Given the relatively small number of perturbations, it was difficult to connect pathways with phenotypes. It is possible that more extensive sets of perturbations may ultimately reveal the underlying molecular mechanisms responsible for particular constraints. However, it is also possible that the complexity of the underlying molecular pathways is too great and multi-faceted to ever fully relate to these constraints in an easily understood manner (Mellis and Raj, 2015). Nevertheless, these constraints and others like them may constitute an effective ‘‘grammar’’ of organoid morphology that one may be able to build upon irrespective of the molecular details. Knowledge of the building blocks of organoid morphologies may also inform generative quantitative models of morphogenesis that could be evaluated for their ability to recapitulate such constraints.

We also found that while some perturbations altered cyst parameters within constraints, others changed the nature of the constraint. Knowledge of which types of perturbations lead to which type of effect might aid in the development of an instruction manual for building designer organoids, potentially existing in very different parts of parameter space than normal organoids. Our framework may reveal the parameters one may be able to manipulate organoids using the rules learned by these systematic perturbations. Such organoids may have properties that make them more useful for particular applications in regenerative medicine or as disease models. It may also be possible, in

principle if not in practice, to destroy a constraint with sufficient perturbation. For example, the right perturbation might completely decouple cyst volume from the number of cells. Future work could search for perturbations with such effects by combining high-throughput drug screens with our detailed quantification of organoid morphologies. With the ability to decouple morphological constraints, we might be able to engineer organoids to adopt entirely novel configurations.

One principal technical challenge in the scaling of approaches such as the one we took here is the extraction of annotations of MDCK cyst structures from microscopy images. Our assumption was that we would need highly accurate annotations to reveal subtle constraints on MDCK cyst morphologies, and those annotations proved difficult to fully automate. For this reason, we chose to build an interface that enabled us to manually correct annotations from any algorithm. Our hope is that this approach and the software is of use to others looking to annotate images, structures, or tissues for which automated solutions have yet to be developed. Deep learning has produced great advances in automatic image segmentation (Moen et al., 2019), and it is possible that the application of these methods, once fully automated and of very high quality, would allow us to obtain much larger numbers of annotations compared with our combination of automated algorithms and manual annotation review. It is also worth considering what level of segmentation accuracy is needed for the question at hand. Future work that quantifies what degree of segmentation accuracy is needed for a given question may guide efforts to develop segmentation algorithms. In addition, it is possible that alternative strategies for culturing or imaging the cysts might make the images easier to segment. One such example would be to plate all MDCK cysts at the same distance from the bottom of the well. Future work could also use the large and highly accurate segmentations produced in this work to train deep learning models specific to this task.

We focused primarily on MDCK cysts for our proof of concept because of their simplicity, both morphologically and in terms of the number of cell types involved (in this case, just one cell type). We also applied our methodology to the more complex enteroid system that has several cell types that interact in various ways; however, the feature set available for each enteroid was relatively less rich due to the complexities of quantifying those features in a complex three-dimensional set of cells. We have demonstrated, in principle, that our approach can determine the ways in which organoid morphologies are either constrained or free to vary. However, it is important to note that more complex organoid systems may have higher degrees of dimensionality and non-linearities that may require more sophisticated approaches and analyses. It will be interesting in the future to apply this framework to such organoids to see what constraints are obeyed, as well as to map the relationship between an organoid's morphological constraints to an organoid's functional characteristics.

STAR★METHODS

Detailed methods are provided in the online version of this paper and include the following:

- KEY RESOURCES TABLE
- RESOURCE AVAILABILITY
  - Lead contact
  - Materials availability
  - Data and code availability
- EXPERIMENTAL MODEL AND SUBJECT DETAILS
  - MDCK cyst culture
- METHOD DETAILS
  - Imaging
  - Drug screen
  - MDCK cyst perturbation experiments
- QUANTIFICATION AND STATISTICAL ANALYSES
  - Morphological quantification from images
  - PCA and linear models
  - Enteroid analysis
  - Figure generation

SUPPLEMENTAL INFORMATION

Supplemental information can be found online at https://doi.org/10.1016/j.cels.2022.05.008.

ACKNOWLEDGMENTS

We thank members of the Raj and Lengner labs for many useful discussions and suggestions. We thank Phil Burnham, Ian Mellis, and Karun Kiani for critical review of the manuscript. We also thank Benjamin Lamarck Emert, Phil Burnham, Yogesh Goyal, Amy Azaria, Karun Kiani, and Ian Dardani for help with fixing 3D annotations. We also thank Réka Hollandi from the Horvath lab for assistance in setting up and running their segmentation software, NucleAIzer. We also thank the Penn High Throughput Screening Core (Sara Cherry, David Schultz, and Christopher Rainville) and Penn Cell and Developmental Biology Microscopy Core (Andrea Stout and Jasmine Zhao) for their help and input. L.E.B. acknowledged support from NIH T32 EB009384. A.J.H. acknowledges support from NIH R35 GM133380, NIH R21 GM132831, and the Penn Institute for Translational Medicine and Therapeutics Pilot Grant. Z.J.G. acknowledges support from the Chan Zuckerberg Biohub Investigator Program, NIH U01 CA199315, and the University of California, San Francisco Center for Cellular Construction DBI-1548297. A.R. acknowledges support from NIH R01 CA238237, NIH Director's Transformative Research Award R01 GM137425, NIH R01 CA232256, NSF CAREER 1350601, NIH P30 CA016520, NIH SPORE P50 CA174523, NIH U01 CA227550, NIH 4DN U01 HL129998, NIH Center for Photogenomics RM1 HG007743, Chan Zuckerberg Initiative Human Cell Atlas 182724, and the Tara Miller Foundation.

AUTHOR CONTRIBUTIONS

L.E.B. conceived of the project, performed the experiments, analyzed the data, and wrote the paper. J.L., C.C., and M.C.D. all provided assistance with manual image annotation. N.S. and M.K.C. performed some preliminary data analysis. I.L. and P.L. provided enteroid data and helpful input on the analysis of such data. A.J.H., J.D.M., and Z.J.G. assisted with crowdsourced image segmentation and also provided valuable intellectual input on the conception of the project. A.R. conceived of the project, provided guidance in data analysis, and wrote the paper.

DECLARATION OF INTERESTS

A.R. receives royalties related to Stellaris RNA FISH probes.

Received: January 13, 2021
Revised: February 15, 2022
Accepted: May 26, 2022
Published: June 14, 2022

Please cite this article in press as: Beck et al., Systematically quantifying morphological features reveals constraints on organoid phenotypes, Cell Systems (2022), https://doi.org/10.1016/j.cels.2022.05.008

REFERENCES

Albanese, A., Swaney, J.M., Yun, D.H., Evans, N.B., Antonucci, J.M., Velasco, S., Sohn, C.H., Arlotta, P., Gehrke, L., and Chung, K. (2020). Multiscale 3D phenotyping of human cerebral organoids. Sci. Rep. *10*, 21487.

Benjamin Erichson, N., Zheng, P., Manohar, K., Brunton, S.L., Kutz, J.N., and Aravkin, A.Y. (2018). Sparse principal component analysis via variable projection. Preprint at arXiv. https://doi.org/10.48550/arXiv.1804.00341.

Cui, M.-L., Copsey, L., Green, A.A., Bangham, J.A., and Coen, E. (2010). Quantitative control of organ shape by combinatorial gene activity. PLoS Biol. *8*, e1000538.

Garreta, E., Kamm, R.D., Chuva de Sousa Lopes, S.M., Lancaster, M.A., Weiss, R., Trepat, X., Hyun, I., and Montserrat, N. (2021). Rethinking organoid technology through bioengineering. Nat. Mater. *20*, 145–155. https://doi.org/10.1038/s41563-020-00804-4.

Gjorevski, N., Sachs, N., Manfrin, A., Giger, S., Bragina, M.E., Ordóñez-Morán, P., Clevers, H., and Lutolf, M.P. (2016). Designer matrices for intestinal stem cell and organoid culture. Nature *539*, 560–564.

Gracz, A.D., Williamson, I.A., Roche, K.C., Johnston, M.J., Wang, F., Wang, Y., Attayek, P.J., Balowski, J., Liu, X.F., Laurenza, R.J., et al. (2015). A high-throughput platform for stem cell niche co-cultures and downstream gene expression analysis. Nat. Cell Biol. *17*, 340–349.

Hafen, E., and Stocker, H. (2003). How are the sizes of cells, organs, and bodies controlled? PLoS Biol. *1*, E86.

Jo, M., Stolz, D.Beer, Esplen, J.E., Dorko, K., Michalopoulos, G.K., and Strom, S.C. (2000). Cross-talk between epidermal growth factor receptor and c-Met signal pathways in transformed cells. J. Biol. Chem. *275*, 8806–8811.

Kanda, T., Sullivan, K.F., and Wahl, G.M. (1998). Histone-GFP Fusion Protein Enables Sensitive Analysis of Chromosome Dynamics in Living Mammalian Cells. Current Biology *8*, 377–385.

Kassis, T., Hernandez-Gordillo, V., Langer, R., and Griffith, L.G. (2019). OrgaQuant: human intestinal organoid localization and quantification using deep convolutional neural networks. Sci. Rep. *9*, 12479.

Kim, J., Koo, B.-K., and Knoblich, J.A. (2020). Human organoids: model systems for human biology and medicine. Nat. Rev. Mol. Cell Biol. *21*, 571–584.

Koo, B., Choi, Baekgyu, Park, Hoewon, and Yoon, K.-J. (2019). Past, present, and future of brain organoid technology. Mol. Cells *42*, 617–627.

Lukonin, I., Serra, D., Challet Meylan, L.C., Volkmann, K., Baaten, J., Zhao, R., Meeusen, S., Colman, K., Maurer, F., Stadler, M.B., et al. (2020). Phenotypic landscape of intestinal organoid regeneration. Nature *586*, 275–280.

Mellis, I.A., and Raj, A. (2015). Half dozen of one, six billion of the other: what can small- and large-scale molecular systems biology learn from one another? Genome Res. *25*, 1466–1472.

Moen, E., Bannon, D., Kudo, T., Graf, W., Covert, M., and Van Valen, D. (2019). Deep learning for cellular image analysis. Nat. Methods *16*, 1233–1246.

Montesano, R., Matsumoto, K., Nakamura, T., and Orci, L. (1991a). Identification of a fibroblast-derived epithelial morphogen as hepatocyte growth factor. Cell *67*, 901–908.

Montesano, R., Schaller, G., and Orci, L. (1991b). Induction of epithelial tubular morphogenesis in vitro by fibroblast-derived soluble factors. Cell *66*, 697–711.

Phipson, B., Er, P.X., Combes, A.N., Forbes, T.A., Howden, S.E., Zappia, L., Yen, H.-J., Lawlor, K.T., Hale, L.J., Sun, J., et al. (2019). Evaluation of variability in human kidney organoids. Nat. Methods *16*, 79–87.

Piccinini, F., Balassa, T., Carbonaro, A., Diosdi, A., Toth, T., Moshkov, N., Tasnadi, E.A., and Horvath, P. (2020). Software tools for 3D nuclei segmentation and quantitative analysis in multicellular aggregates. Comp. Struct. Biotechnol. J. *18*, 1287–1300.

Savage, V.M., Allen, A.P., Brown, J.H., Gillooly, J.F., Herman, A.B., Woodruff, W.H., and West, G.B. (2007). Scaling of number, size, and metabolic rate of cells with body size in mammals. Proc. Natl. Acad. Sci. USA *104*, 4718–4723.

Sidhaye, J., and Knoblich, J.A. (2021). Brain organoids: an ensemble of bioassays to investigate human neurodevelopment and disease. Cell Death Differ. *28*, 52–67. https://doi.org/10.1038/s41418-020-0566-4.

Stephens, G.J., Johnson-Kerner, B., Bialek, W., and Ryu, W.S. (2008). Dimensionality and dynamics in the behavior of *C. elegans*. PLoS Comp. Biol. *4*, e1000028.

Stringer, C., Wang, T., Michaelos, M., and Pachitariu, M. (2020). Cellpose: a generalist algorithm for cellular segmentation. Nat. Methods *18*, 100–106. https://doi.org/10.1038/s41592-020-01018-x.

Vasquez, C.G., Vachharajani, V.T., Garzon-Coral, C., and Dunn, A.R. (2021). Physical basis for the determination of lumen shape in a simple epithelium. Nat. Commun. *12*, 5608.

Volpato, V., Smith, J., Sandor, C., Ried, J.S., Baud, A., Handel, A., Newey, S.E., Wessely, F., Attar, M., Whiteley, E., et al. (2018). Reproducibility of molecular phenotypes after long-term differentiation to human iPSC-derived neurons: a multi-site omics study. Stem Cell Rep. *11*, 897–911.

Yin, X., Farin, H.F., van Es, J.H., Clevers, H., Langer, R., and Karp, J.M. (2014). Niche-independent high-purity cultures of Lgr5+ intestinal stem cells and their progeny. Nat. Methods *11*, 106–112.

Yost, E.A., Mervine, S.M., Sabo, J.L., Hynes, T.R., and Berlot, C.H. (2007). Live Cell Analysis of G Protein beta5 Complex Formation, Function, and Targeting. Molecular Pharmacology *72*, 812–825.

Please cite this article in press as: Beck et al., Systematically quantifying morphological features reveals constraints on organoid phenotypes, Cell Systems (2022), https://doi.org/10.1016/j.cels.2022.05.008

STAR★METHODS

KEY RESOURCES TABLE

REAGENT or RESOURCE	SOURCE	IDENTIFIER
Deposited data		
all raw and analyzed data, scripts to generate all figures	this paper	https://www.dropbox.com/sh/u2tqi7w235b63v6/AADyq-LfaE2HS97lLfYCPBP4a?dl=0
Experimental models: Cell lines		
Canine: MDCK-II cell line	MilleporeSigma	Cat#00062107--1VL
Recombinant DNA		
H2B-GFP plasmid	Kanda et al., 1998	Addgene, Cat#11680
mem-mCherry plasmid	Yost et al., 2007	Addgene, Cat#55779
Software and algorithms		
organoids2 - repository containing pipeline for extracting morphological features from microscopy images	this paper	https://doi.org/10.5281/zenodo.6379616
rajlabimagetools - repository containing image analysis tools, required by organoids2	this paper	https://doi.org/10.5281/zenodo.6379614
Cellpose	Stringer et al., 2020	https://www.cellpose.org/

RESOURCE AVAILABILITY

Lead contact

Further information and requests for resources and reagents should be directed to and will be fulfilled by the lead contact, Arjun Raj (arjunrajlab@gmail.com).

Materials availability

This study did not generate new unique reagents.

Data and code availability

- All data have been deposited at https://www.dropbox.com/sh/u2tqi7w235b63v6/AADyq-LfaE2HS97lLfYCPBP4a?dl=0 and are publicly available as of the date of publication. DOIs are listed in the key resources table.
- All original code developed for the pipeline to quantify morphological features from microscopy images has been deposited at https://github.com/arjunrajlaboratory/organoids2 and https://github.com/arjunrajlaboratory/rajlabimagetools and is publicly available as of the date of publication. All original code developed to create all figures from morphological features data has been deposited at https://www.dropbox.com/sh/u2tqi7w235b63v6/AADyq-LfaE2HS97lLfYCPBP4a?dl=0 and is publicly available as of the date of publication. DOIs are listed in the key resources table.
- Any additional information required to reanalyze the data reported in this paper is available from the lead contact upon request.

EXPERIMENTAL MODEL AND SUBJECT DETAILS

MDCK cyst culture

Madin-Darby Canine Kidney-II cells (MilliporeSigma, 00062107--1VL) were maintained by culturing them in 2D on traditional 10 cm cell culture-coated dishes (Corning, 353003). The media for both the adherent 2D cells and cysts was MEM media (MediaTech, MT10--010--CM) with 10% Fetal Bovine Serum (Fisher, 16000044) and 1X Penicillin-Streptomycin (Invitrogen, 15140122). When the cells were between 30-70% confluence there were dissociated to make cysts. The cells were briefly washed with 5 mL of DPBS (Gibco, 14190136). Then, 1 mL of 0.25% Trypsin-EDTA (Gibco, 25200056) was added and the plate was incubated at 37 °C, 5% CO_2 for 10-15 minutes. The trypsin was inactivated with 9 mL of media and the solution was pipetted over the dish three times to ensure all cells detached. The cells were pelleted for 2 minutes at 1000 rpm and then suspended in 500 μL to 1 mL media. The cell concentration was quantified using a BioRad TC20 Automated Cell Counter. The cells were added to ice-cold thawed Matrigel (Corning, 354234) at a concentration of 25,000 cells/mL. The middle of a well of a Nunc Lab-Tek 8-well Chambered Coverglass (Fisher, 12-565-470) was coated with 5 μL of pure Matrigel. Then, 25 μL of the cell-Matrigel suspension was overlaid on top of the coating. The chamber was incubated at 37 °C, 5% CO_2 for 30 minutes to solidify the Matrigel. Then, 200 μL of media was added

Please cite this article in press as: Beck et al., Systematically quantifying morphological features reveals constraints on organoid phenotypes, Cell Systems (2022), https://doi.org/10.1016/j.cels.2022.05.008

on top of the solidified Matrigel. The cysts were returned to the 37 °C, 5% CO_2 incubator and cultured for 3-17 days. The media was replaced every other day.

METHOD DETAILS

Imaging

MDCK cyst fixation and staining was performed at room temperature with two brief washes with 1X PBS (Ambion, AM9624) between each step. When the cysts were ready to be imaged they were fixed in their culture chambers with 1.85% formaldehyde (MilliporeSigma, F1635-500ML) in PBS for 30 minutes. They were permeabilized with 0.1% Triton X-100 (MilliporeSigma, T8787-100mL) in PBS overnight. The cysts were then blocked with 5% Bovine Serum Albumin (MilliporeSigma, A7906-100G) in PBS for 1 hour. The cysts were then incubated with 1:15 488-phalloidin (Invitrogen, A12379) and 1:30 DAPI (Fisher, D3571) in PBS for at least 6 hours before imaging. The cysts were imaged on a Zeiss Laser Scanning 710 Confocal Microscope using a 40X objective (Zeiss, water immersion, 1.1 NA, long working distance, LD C-Apochromat), 405 nm diode laser (Zeiss), and 488 nm argon-ion laser (LASOS). Each cyst was imaged from the bottom to a depth clearly beyond the middle point of the cyst. Cysts that were too far from the glass to image that deeply were not imaged.

Drug screen

We first established MDCK-II cells with stable integration of GFP nuclear and mCherry cell membrane markers. The day before we planned to transfect the cells we plated them so that the cells would be ~80% confluent at the time of transfection. The cells were cultured in media without antibiotics. The following day, we used Lipofectamine 2000 (Invitrogen, 11668019) to transfect the cells with H2B-GFP plasmid (https://www.addgene.org/11680/). Two days after transfection, we replaced the media with media containing penicillin, streptoymycin, and G418 (Mediatech, MT30-234-CR). We changed the media every other day. One week after transfection we single cell bottlenecked the cells. We then followed the same approach to transfect the cells with mem-mCherry plasmid (https://www.addgene.org/55779/).

To conduct the drug screen, we used Matrix WellMate to plate Matrigel with 35,000 cells/mL into 384-well plates. We then centrifuged the plates at 300 rpm for 1 minute to ensure the Matrigel-cell suspension fell to the bottom of the well. We polymerized the Matrigel by placing the plates in a 37 °C, 5% CO2 incubator for 30 minutes. We then added 20 μL of media with 20 mM HEPES and drug using a Perkin Elmer Janus Modular Dispensing Tool. The cysts were cultured for 7 days at 37 °C, 5% CO2.

To image the cysts, we fixed them with 20 μL of 8% formaldehyde for 30 minutes at room temperature. We washed the plates with PBS and then stained them with 1:2500 Hoescht in PBS overnight. We used a Molecular Device's ImageXpress Micro XLS Widefield High-Content Analysis System to image each plate at 10X. We took 4 images, each at the height determined by the autofocus software, per well.

We then quantified the effect of each drug on cyst size using custom MATLAB scripts. First, we combined the three image channels. We then Gaussian filtered the image and binarized it using Otsu's method. We then obtained the boundary of cysts by obtaining the boundary of all objects in the binary image that were bigger than 50 pixels and smaller than 1500 pixels. We calculated the area of each cyst using MATLAB's regionprops function. We then calculated the average fold change in cyst area for each drug by dividing the average cyst area for the drug by the average cyst area for all control cyst from the same plate. We similarly calculate the z-score for each drug.

To identify hits that made the cysts larger, we found drugs in common between the list of top 100 drugs by fold change and the list of top 100 drugs by cyst area. To identify hits that made the cyst smaller, we found drugs in common between the list of both 100 drugs by fold chance and the list of bottom 100 drugs by cyst area.

MDCK cyst perturbation experiments

MDCK cysts were cultured using the above technique with the following exceptions. For drug perturbations, cysts were cultured in media containing drug throughout their entire growth (Table S2). Media was replaced every other day. For the high cell density perturbation, the cysts were plated from a cell-Matrigel suspension containing 100,000 cells/mL. For the 70% Matrigel perturbation, a solution of 70% Matrigel diluted with MDCK media was used to both coat the plate and culture the cysts. Cysts were fixed and imaged on the 9th day using the protocols described above. Note that in the drug screen the cysts were fixed on the 7th day (because the screening facility was concerned that longer timepoints would risk media evaporation). However, to more easily compare the effects of drug perturbations with age perturbations we decided to use the same reference age (9 days).

QUANTIFICATION AND STATISTICAL ANALYSES

Morphological quantification from images

We wrote a custom MATLAB pipeline (https://github.com/arjunrajlaboratory/organoids2) to measure cyst morphological features from microscopy images by 3D segmenting the boundaries of the whole cyst and each of its lumens and nuclei. To segment the cyst and lumen boundaries our general approach was to guess the boundary on each image slice using the phalloidin image and then manually correct the boundary as needed. To guess the cyst boundary on each slice we set an empty corner of the image as the starting boundary and expanded that boundary outward until the intensity of those pixels was above a user-defined threshold.

Please cite this article in press as: Beck et al., Systematically quantifying morphological features reveals constraints on organoid phenotypes, Cell Systems (2022), https://doi.org/10.1016/j.cels.2022.05.008

We applied the same approach to guess the lumen boundaries, except we identified the starting point as the largest object after the slice had been processed with a Laplacian of Gaussian edge detector. We then manually reviewed these 2D boundaries and corrected them as needed (Figure S2B). Once these 2D boundaries were finalized they were combined to form 3D boundaries. We obtained 3D cyst boundaries by assuming all 2D cyst annotations belonged to the same object. We obtained 3D lumen boundaries by computationally identifying which boundaries touched one another when stacked in 3D. To 2D segment the nuclear boundaries we used cellpose to segment the nuclei on the original image slices. We also sliced the image stack orthogonally from its original slicing, such that moving from slice-to-slice moves left-right across the cyst, rather than up-down. We also used cellpose to segment the nuclei on these orthogonal slices. We then used the orthogonal 2D segmentations to guess which original 2D segmentations were connected to one another. We then manually reviewed these 3D connections and corrected them as needed (Figure S3C).

Once we had 3D boundaries for the cyst, lumens, and nuclei, we wrote custom analyses to measure morphological features of size, shape, and number for each cyst (Table S1). For cysts with multiple lumens, we took the mean across all lumens. For cysts with multiple nuclei, we took both the mean and the standard deviation across all nuclei.

PCA and linear models

In order to run PCA we first standardized the units of our features. We took the cube root of all volume features, the square root of all surface area features, and the inverse of the number of lumens. We then z-score normalized each feature. We ran PCA using the prcomp function from the R's stats package (https://www.rdocumentation.org/packages/stats/versions/3.6.2). To estimate how much variance we could expect to be explained due to chance, we also ran PCA on randomized data. To randomize the data, we shuffled each column of a table where each row represents one cyst/enteroid and each column represents one morphological feature.

We fit linear models to various pairs of morphological features using ggplot2 (https://ggplot2.tidyverse.org/) and R's stats package.

Enteroid analysis

Data on unperturbed and perturbed enteroids was provided by Ilya Lukonin and Prisca Liberali. Details on enteroid generation, culture, imaging, and image analysis can be found in their 2020 publication in Nature.

Figure generation

We used MATLAB to format images for all figures. All other analyses were done in R. We used a selection of color-blind friendly colors for Figures 2, 3, and 4 from https://personal.sron.nl/~pault/.